



Article

Fractional-Order Gas Film Model

Xu Tang , Ying Luo * and Bin Han

School of Mechanical Science and Engineering, Huazhong University of Science and Technology, Wuhan 430074, China

* Correspondence: ying.luo@hust.edu.cn

Abstract: In this paper, a fractional-order model of the gas film is proposed for the dynamic characteristics of an air bearing. Based on the dynamic characteristics common between gas film and viscoelastic body, the idea of the fractional-order equivalent modeling of the dynamic characteristics of the gas film is presented to improve the modeling accuracy. Four fractional-order gas film (FOGF) models are introduced based on generalization of traditional viscoelastic models. The analysis of the characteristics of the FOGF models shows that the FOGF model can capture more complex dynamic characteristics and fit the real dynamic data of the gas film better than traditional models. A genetic algorithm particle swarm optimization (GA-PSO) method is used for parameter identification of the proposed models. The experimental results tested on the air bearing motion platform show that the FOGF models are superior in accuracy to the traditional equivalent models for the gas film. In particular, the fractional-order Maxwell gas film (FOMGF) model has the best capture accuracy compared to the other FOGF models and traditional models.

Keywords: fractional-order model; gas film model; dynamic characteristics of the air bearing



Citation: Tang, X.; Luo, Y.; Han, B. Fractional-Order Gas Film Model. *Fractal Fract.* **2022**, *6*, 561. <https://doi.org/10.3390/fractalfract6100561>

Academic Editors: Simona Coman, Cristian Boldisor and Jordan Hristov

Received: 23 July 2022

Accepted: 21 September 2022

Published: 3 October 2022

Publisher's Note: MDPI stays neutral with regard to jurisdictional claims in published maps and institutional affiliations.



Copyright: © 2022 by the authors. Licensee MDPI, Basel, Switzerland. This article is an open access article distributed under the terms and conditions of the Creative Commons Attribution (CC BY) license (<https://creativecommons.org/licenses/by/4.0/>).

1. Introduction

Compared with the contact bearing, the air bearing has the advantages of high speed, high precision, low power consumption, and a long service life. It can meet the requirements of ultra-precision equipment such as IC manufacturing and optical element processing for motion support. Since the concept of air lubrication was put forward in the Mid-19th Century [1], the air bearing has gradually shifted from theoretical research to practical design and application, such as ultra-precision machine tools [2–4], measuring instruments [5], computer storage equipment [6,7], and other ultra-precision fields.

The research core of the air bearing is the dynamic/static characteristics and stability. The air bearing fluid follows the Navier–Stokes (N-S) equation of macroscopic fluid motion based on the continuity assumption. The N–S equation is a nonlinear partial differential equation, and there is no general method to solve it accurately at present. Based on some assumptions, Harrison [8] simplified the N-S equation, deduced the one-dimensional compressible Reynolds equation with infinite width, and established the foundation of the early hydrostatic gas lubrication theory. The current research on dynamic and static characteristics needs to find the solution of the Reynolds equation [9]. The solution of the static characteristics mainly includes the finite element method [10,11], finite difference method [12–15], and finite volume method [16,17]. To solve the dynamic characteristics, the primary methods include the perturbation method [18–21], finite element method [22–24], numerical calculation [10,25–28], approximate solution [29], and finite difference method [20,21]. These methods are mainly based on fluid theory, and the dynamic/static characteristics of the air bearing are obtained by solving the N-S equation. The complicated methods are inconvenient to model the air bearing in the control system.

The complex stiffness characteristics of the air bearing can be obtained by the perturbation method, finite element method, and so on. It can be found that the gas film formed between air floating platforms has similar dynamic and static characteristics to

viscoelastic materials. On this basis, the gas film of the air bearing system can be abstracted as a nonlinear dynamic model system. Furthermore, the gas film of the air bearing can be abstracted as a unique viscoelastic body [30]. Generally, the viscoelastic behavior is described as a combination of ideal elastic and viscous components. In the application field of air bearings, some scholars use a simple spring–damper (SD model) system to model and control the system equivalently [31,32]. The dynamic characteristics of the gas film have frequency correlation and significant differences under different air flotation conditions, which limits the fitting effect of the simple model. Al-Bender et al. [33,34] introduced a more complex spring-damping system (Zener model, etc.) for equivalent modeling. However, these traditional viscoelastic models still have undesired errors and limitations in the equivalence of gas film characteristics.

Fractional calculus is an effective mathematical tool. It has been shown by many studies that fractional-order models can simulate complex systems well, especially in the modeling of nonlinear dynamic systems. The fractional calculus tool is introduced into the viscoelastic model to better explain some complex viscoelastic properties. Sahraoui et al. [35] used the fractional-order Zener model to characterize viscoelastic foam. Liang et al. [36] used the fractional-order Maxwell model to describe the ultra-low creep behavior of concrete. The method also has been successfully applied to other viscoelastic materials [37–39]. It should be a reasonable and feasible method to accurately describe the nonlinear dynamic characteristics of the air bearing by using the fractional-order model.

In this paper, four fractional-order gas film (FOGF) models are proposed to accurately capture the dynamic characteristics of the gas film. The FOGF models have more variable dynamic characteristics, which can better match the dynamic characteristics of the gas film in different states. Based on the proposed FOGF models, a parameter identification method based on experimental measurement is also proposed. Compared with the existing equivalent models, the experimental results show that the FOGF models can effectively improve the fitting accuracy of the transfer function. The FO-Maxwell gas film (FOMGF) model has the best fitting accuracy compared to the other FOGF models and traditional models.

The main contributions of this paper include the following: (1) The idea of fractional-order modeling is introduced to the equivalent modeling of the gas film, and four fractional-order gas film (FOGF) models are established. (2) The dynamic characteristics of the established FOGF models are analyzed and compared with existing traditional models to show the advantages of the proposed models. (3) The genetic algorithm and particle swarm optimization (GA-PSO) are presented to identify the parameters of the FOGF models. (4) The experimental verification is carried out on the H-type air bearing floating motion platform, and the modeling accuracy of the proposed FOGF models is compared with that of the existing equivalent models.

The structure of this paper is as follows: Section 2 introduces the dynamic characteristics of the gas film. Section 3 introduces the specific implementation and characteristics of the FOGF models. Section 4 introduces the parameter identification method of the FOGF models. In Section 5, experiments conducted on an H-type air bearing floating motion platform are demonstrated, and the FOGF models are compared with the conventional spring-damped model for modeling accuracy. The conclusion is provided in Section 6.

2. Gas Film Dynamic Characteristics

As shown in Figure 1, to better discuss the dynamic characteristics of the gas film, the dynamic characteristics of an infinite flat air bearing are obtained by the perturbation method.

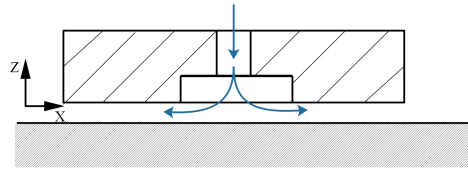


Figure 1. Schematic diagram of gas film lubrication.

In the derivation process, the basic assumptions are: (1) isothermal; (2) the gas flow is laminar; (3) ignoring the inertia force of the gas flow; (4) there is no slip phenomenon at the contact boundary between the gas and solid; (5) the air bearing support object is a rigid body and has no tangential relative motion.

From the Navier–Stokes (N-S) equation, the Reynolds equation for the gas film can be derived [28]:

$$\frac{\partial}{\partial x}(\rho h^3 \frac{\partial p}{\partial x}) + \frac{\partial}{\partial y}(\rho h^3 \frac{\partial p}{\partial y}) + 12\delta\mu q = 12\mu \frac{\partial}{\partial t}(\rho h) \quad (1)$$

where p is the pressure distribution in the gas film, h is the thickness of the gas film, ρ is the gas density, μ is the dynamic viscosity of the gas, q is the flow at the orifice, t is the time, and δ is the Kronecker number. When considering the slight disturbance of the gas film, the gas film thickness at any time can be expressed as:

$$h = h_0 + \Delta h = h_0 + h_1 e^{j\omega t} \quad (j = \sqrt{-1}, \quad h_1 \ll h_0) \quad (2)$$

where $\omega = 2\pi f$, f is the frequency, h_0 is the initial film thickness, and Δh and $h_1 e^{j\omega t}$ are the disturbance quantities. From the change of the gas film thickness, the flow rate equation of the air bearing can be obtained:

$$q = q_0 + \left. \frac{\partial q}{\partial p} \right|_{p=p_0} \Delta p \quad (3)$$

where q is the flow rate, p is the air pressure, p_0 is the air pressure in the state of the gas film h_0 state, and Δp is the air pressure change caused by the disturbance. Based on the Reynolds equation, considering gas compressibility, the equation can be deduced as follows:

$$\frac{\partial}{\partial x}(h^3 \frac{\partial p^2}{\partial x}) + \frac{\partial}{\partial y}(h^3 \frac{\partial p^2}{\partial y}) + 24\delta\mu RT q = 24\mu \frac{\partial}{\partial t}(\rho h) \quad (4)$$

where R is the molar gas constant and T is the absolute temperature. Assume that the change in the frequency of Δp and Δh is the same. The disturbance equation can be solved as follows:

$$\begin{aligned} & 2 \left[\frac{\partial}{\partial x} (h_0^3 \frac{\partial p_0 \Delta p / \Delta h}{\partial x}) + \frac{\partial}{\partial y} (h_0^3 \frac{\partial p_0 \Delta p / \Delta h}{\partial y}) \right] + 24\delta\mu RT \frac{\partial q \Delta p / \Delta h}{\partial p} + \\ & 3 \left[\frac{\partial}{\partial x} (h_0^2 \frac{\partial p_0^2}{\partial x}) + \frac{\partial}{\partial y} (h_0^2 \frac{\partial p_0^2}{\partial y}) \right] = 24\mu (w \Delta p / \Delta h + p_0 w) \cdot j \end{aligned} \quad (5)$$

The solution of Equation (5) can be expressed as:

$$\frac{\Delta p}{\Delta h} = \text{Real}(w, p_0, h_0) + \text{Imag}(w, p_0, h_0) \cdot j \quad (6)$$

where $\text{Real}(w, p_0, h_0)$ is the real part of the solution and $\text{Imag}(w, p_0, h_0)$ is the imaginary part of the solution. Equation (6) is written in complex stiffness form as:

$$K^* = \int \text{Real}(w, p_0, h_0) dA + j \cdot \int \text{Imag}(w, p_0, h_0) dA \quad (7)$$

where K^* is the complex stiffness. Based on Equation (4) and perturbation theory, the general solution of the two-dimensional gas film can be obtained as follows:

$$\Delta p = \frac{P_a \Delta h}{h_0} \left[\frac{ch(\sqrt{12\mu j\omega/P_a h_0^2} x)}{ch(\sqrt{12\mu j\omega/P_a h_0^2} B/2)} - 1 \right] \tag{8}$$

where $ch()$ stands for the hyperbolic cosine function, B is the plate width, and P_a is the boundary pressure. Introduce the extrusion number:

$$\sigma = \frac{12\mu B^2 \omega}{P_a h_0^2} \tag{9}$$

The dynamic bearing capacity is obtained by integrating the dynamic bearing pressure generated by extrusion on the plate:

$$\Delta F = L \int_{-B/2}^{B/2} \Delta p dx = LB P_a \frac{\Delta h}{h_0} \left[\frac{2th(\sqrt{\sigma} e^{\pi j/4}/2)}{\sqrt{\sigma} e^{\pi j/4}} - 1 \right] \tag{10}$$

where $th()$ stands for the hyperbolic tangent function and L is the length of the plate. According to Equation (10), the dynamic characteristic stiffness K and damping C of the infinite flat air bearing are as follows:

$$K = \frac{LB P_a}{h_0} \text{Real} \left[1 - \frac{2th(\sqrt{\sigma} e^{\pi j/4}/2)}{\sqrt{\sigma} e^{\pi j/4}} \right], C = \frac{LB P_a}{h_0 \omega} \text{Imag} \left[1 - \frac{2th(\sqrt{\sigma} e^{\pi j/4}/2)}{\sqrt{\sigma} e^{\pi j/4}} \right] \tag{11}$$

where $\text{Real}[x]$ represents the real part of x and $\text{Imag}[x]$ represents the real part of x . Making it dimensionless, the dimensionless stiffness \hat{K} and dimensionless damping \hat{C} are obtained:

$$\hat{K} = \frac{K h_0}{LB P_a} = \text{Real} \left[1 - \frac{2th(\sqrt{\sigma} e^{\pi j/4}/2)}{\sqrt{\sigma} e^{\pi j/4}} \right], \hat{C} = \frac{C h_0^3}{12\mu LB^3} = \sigma^{-1} \text{Imag} \left[1 - \frac{2th(\sqrt{\sigma} e^{\pi j/4}/2)}{\sqrt{\sigma} e^{\pi j/4}} \right] \tag{12}$$

where $\text{Real}[x]$ represents the real part of x and $\text{Imag}[x]$ represents the real part of x . The expressions of the stiffness and damping of the infinite plate air bearing based on the perturbation method are obtained as shown in Equation (12). Due to many assumptions, the derived results can only be solved to obtain the approximate solution of the dynamic characteristics of the air film under certain conditions. As shown in Figure 2, it can still be seen from this result that the dynamic characteristics of the gas film are essentially nonlinear and unsteady, and there is a frequency correlation. The gas film characteristics are similar to those of the viscoelastic body [38–40].

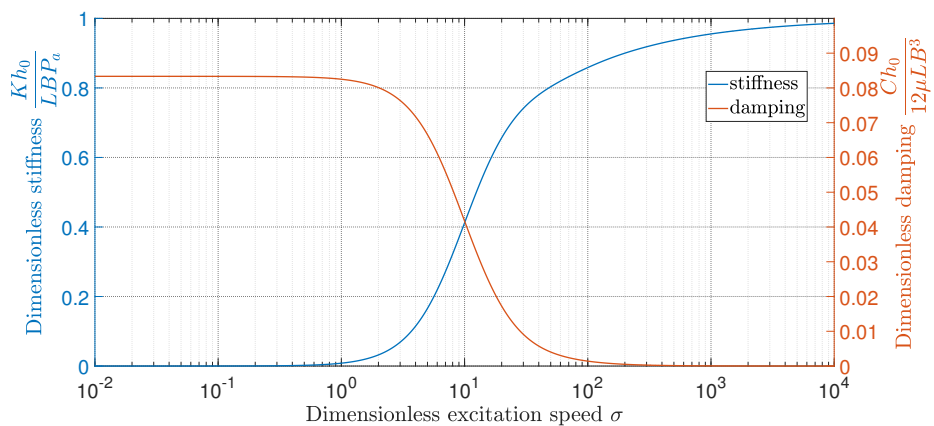


Figure 2. Dimensionless dynamic stiffness and damping characteristics of the gas film.

In fact, the dynamic characteristics of the gas film are affected by different supporting structures, air supply pressure, film thickness, disturbance amplitude, and so on. The gas film can show more complex characteristics than the viscoelastic body. Zhu [41] discussed the influence of the air film thickness, air supply pressure, and disturbance amplitude on the dynamic characteristics of the air bearing. Bhat et al. [9] presented the influence of different pore sizes on the gas film characteristics. Arghir et al. [33] showed the effect of gas compressibility on the gas film properties. Yoshimoto et al. [25] discussed the influence of different air supply modes on the gas film characteristics. Long [42] investigated the effect of different throttling types on the gas film dynamic characteristics.

As shown in Figure 3 [41], it can be seen that the air supply pressure can greatly change the damping variation characteristics of the low frequency. Figure 4 [41] shows that the film thickness can greatly change the damping change characteristics of medium and low frequencies. It can be seen from Figure 5 [9] that the pore size can affect the upward trend of stiffness (produce the minimum peak of stiffness) and even produce negative damping. According to these scholars' discussion on the film characteristics of the air bearing, it can be seen that, besides the disturbance amplitude, other factors, such as the gas film thickness, also have an influence on the dynamic characteristics. The dynamic characteristics of the gas film not only have a frequency correlation, but also have great differences under different conditions. In the past modeling of multibody dynamics, the gas film was often simplified as a linear and steady spring damping element. The simple equivalence cannot effectively capture the dynamic characteristics of the gas film under various conditions. The motion control accuracy of ultra-precision air flotation equipment is limited to some extent. Therefore, it is necessary to introduce an equivalent model that can capture more dynamic characteristics of the gas film.

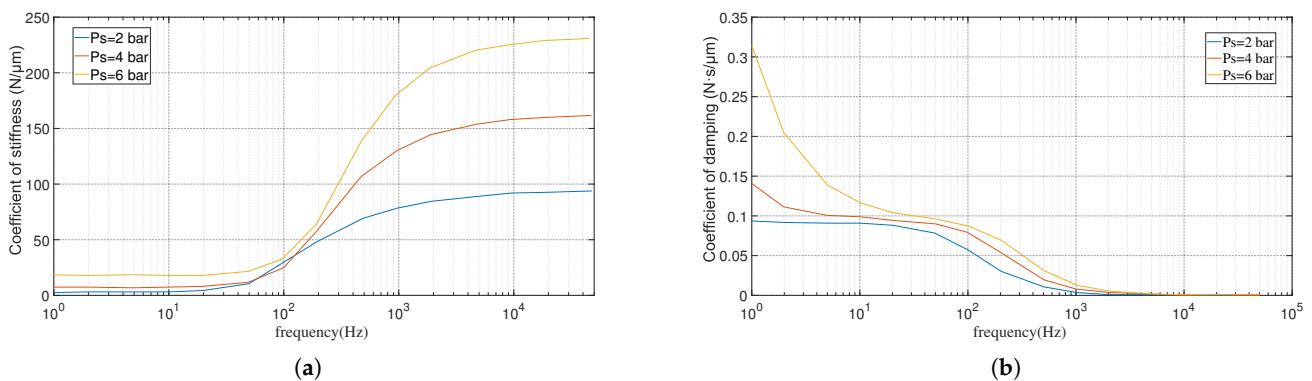


Figure 3. The dynamic characteristics of the gas film under different air supply pressures [41] (orifice diameter = 0.3 mm, gas film thickness = 10 μm). (a) Change of dynamic stiffness with air supply pressures. (b) Change of damping with air supply pressures.

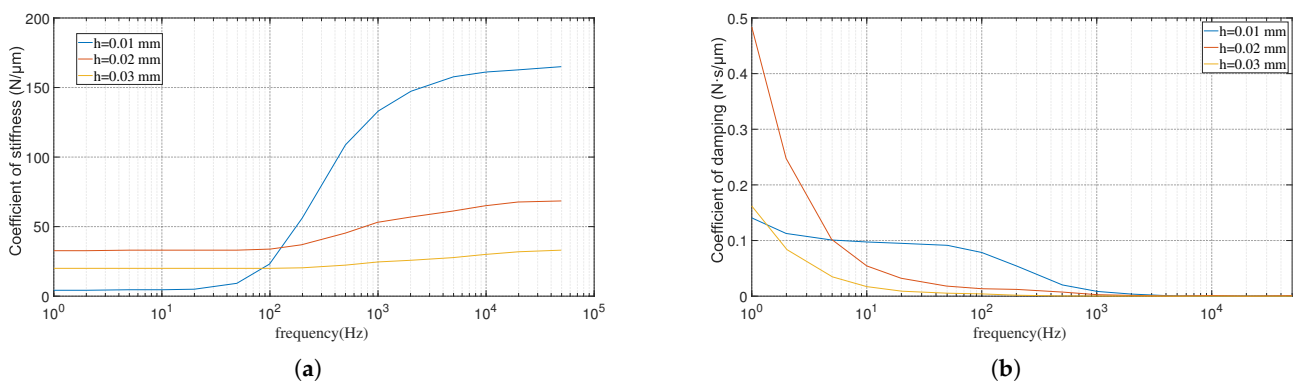


Figure 4. The dynamic characteristics of the gas film under different film thicknesses [41] (orifice diameter = 0.3 mm, gas supply pressure = 4 Mpa). (a) Change of dynamic stiffness with film thickness. (b) Change of damping with film thickness.

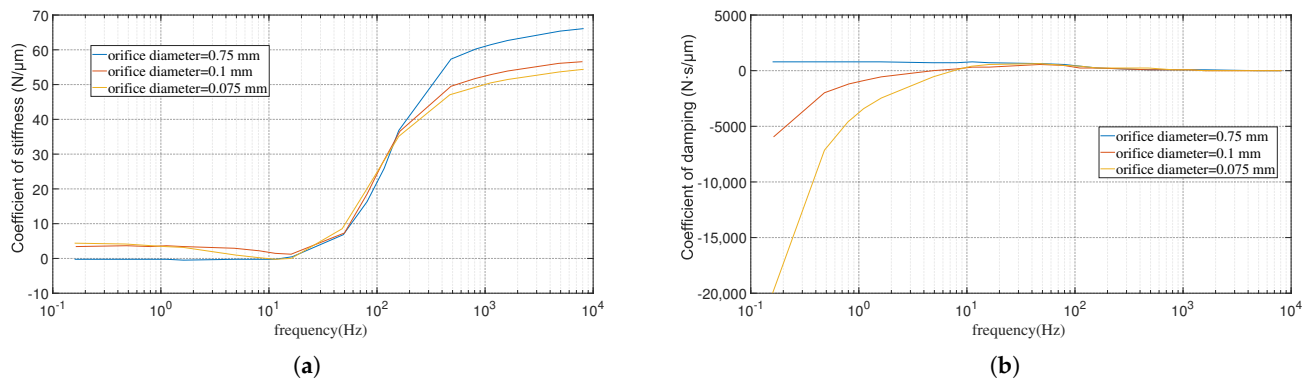


Figure 5. The dynamic characteristics of the gas film under different orifice diameters [9] (gas film thickness = 15 μm , gas supply pressure = 4.8 Mpa). (a) Change of dynamic stiffness with orifice diameter. (b) Change of damping with orifice diameter. Reprinted with permission from ref. [9]. Copyright 2022 Elsevier.

3. Fractional Calculus Definition and Fractional-Order Model

In this section, four fractional-order gas film (FOGF) models are proposed and the stiffness and damping characteristics of the established FOGF models are analyzed.

3.1. Fractional Calculus Definition

Fractional calculus is an important branch of mathematics. Along with the continuous research of the theory of fractional calculus, researchers found that fractional calculus can depict many non-classical phenomena in natural science and engineering applications [43,44]. Generally speaking, obtaining the analytical solutions to most fractional differential equations is difficult. With the development of computers in recent years, numerical methods such as the finite element method [45–47], variational iteration method [47,48], finite difference method [49], operational matrix method [50], and B-spline collocation method [51] have been used to solve fractional models. Shymanskyi et al. [45] calculated the main relationship of the rheological properties of biomaterials with a fractal structure by the finite element method. The fractional model can be solved discretely by the impulse response invariance method.

The common definitions of fractional operators are the Riemann–Liouville (R-L) definition, Caputo definition, and Grunwald–Letnikov (GL) definition [52–54]. In this paper, the common Caputo definition was adopted (Equation (13)), which has the advantage that the physical meaning of the initial value is the same as that of integral calculus.

$$D_t^\alpha f(t) = \frac{d^\alpha f(t)}{dt^\alpha} = \frac{1}{\Gamma(n-\alpha)} \int_0^t \frac{f^{(n)}(\tau)}{(t-\tau)^{\alpha+1-n}} d\tau \quad (13)$$

where $n-1 \leq \alpha < n$ (n is an integer), α is the order of the fractional derivative, and $f^{(n)}(\tau)$ is the n th derivative of $f(\tau)$. $\Gamma(x)$ is the Gamma function:

$$\Gamma(x) = \int_0^\infty e^{-t} t^{x-1} dt \quad (14)$$

These operators can be expressed mathematically for any order α as follows [55]:

$${}_t D_t^\alpha = \begin{cases} \frac{d^\alpha}{dt^\alpha} & \text{Re}(\alpha) > 0 \\ 1, & \text{Re}(\alpha) = 0 \\ \int_{t_0}^t (d\tau)^{-\alpha}, & \text{Re}(\alpha) < 0 \end{cases} \quad (15)$$

3.2. Model Component

The equivalent model of the fractional gas film is composed of the spring, damper, and fractional-damper, as shown in Figure 6. Its general expression is as follows:

$$F(t) = \eta D_t^\alpha x(t) \tag{16}$$

where η is the stiffness or damping coefficient, $D_t^\alpha x(t)$ is the α -order derivative of displacement $x(t)$ with respect to time t . When $\alpha = 0$, the model is a typical hooker spring, as shown in Figure 6a. When $\alpha = 1$, the model is a typical damper, as shown in Figure 6b. When $\alpha \neq n$ (n is an integer), it is a fractional element, as shown in Figure 6c.

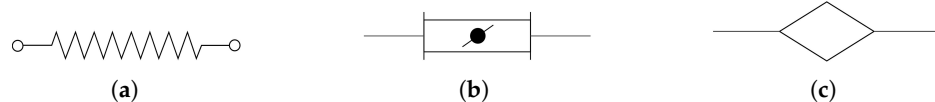


Figure 6. Model component. (a) Spring element. (b) Damper element. (c) Fractional-damper element.

The results of the Laplace transformation of the model elements are as follows:

$$F(s) = \frac{\eta X(s)}{s^\alpha} \tag{17}$$

The fluid shows viscoelasticity in the practical application of some materials or devices, and its mechanical properties show the characteristics of the spring and damper. This physical characteristic can be described as the fractional-damper [56]. The fractional-damper describes the evolution of the physical system with loss, and the fractional order of the derivative represents the share of the system state that persists in the whole evolution process. Figure 7 shows the transfer function curves of a single component after the Laplace transformation in different α orders when the correlation coefficient $\eta = 1$. The fractional-damper can have the properties between the spring and the damper. The establishment of the fractional-damper fills the gap between the spring and damper properties. The fractional-damper can be considered when the model composed of the spring and damper cannot accurately characterize the material properties. A separate fractional-damper cannot represent the substantial viscoelastic body, so it needs to be combined with other components to establish a model. The model established by the fractional-damper can represent more complex viscoelastic behavior with the change of order. The intermediate property of the fractional-damper brings excellent convenience to the modeling of the complex characteristics of the gas film.

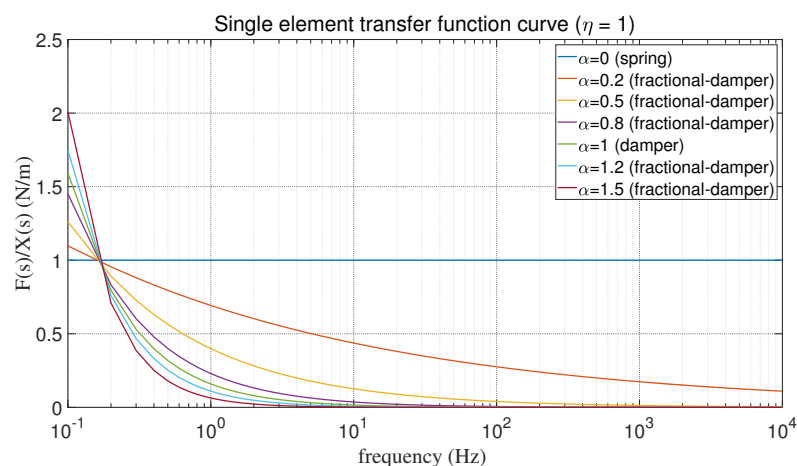


Figure 7. Transfer function curve of a single model element.

3.3. Fractional-Order Gas Film Models

In this paper, based on the traditional model, four FOGF models (Figure 8) are established: FO-Zener gas film model, FO-Maxwell gas film model, FO-three-parameter gas film model, FO-Burgess gas film model. The purpose is to show that the FOGF models are more suitable for capturing the gas film characteristics than the traditional models.

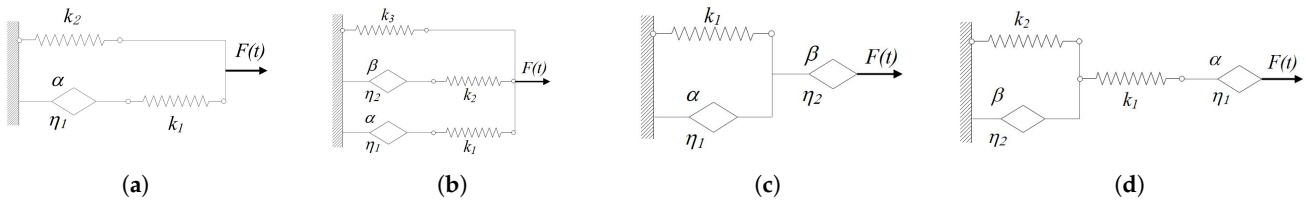


Figure 8. FOGF models. (a) FOZGF model. (b) FOMGF model. (c) FOTGF model. (d) FOBGF model.

3.3.1. Fractional-Order Zener Gas Film Model

The structure of the fractional-order Zener gas film (FOZGF) model is shown in Figure 8a. The FOZGF model is obtained by replacing the damper of the Zener model with the fractional-damper. As for this model, it can be obtained by the Laplace transformation and Euler formula, where its transfer function expression is as follows:

$$Z = \frac{F(w)}{X(w)} = \frac{k_1 \eta_1 w^\alpha \cos(\frac{\pi}{2} \alpha) + k_1 \eta_1 w^\alpha \sin(\frac{\pi}{2} \alpha) \cdot j}{k_1 + \eta_1 w^\alpha \cos(\frac{\pi}{2} \alpha) + \eta_1 w^\alpha \sin(\frac{\pi}{2} \alpha) \cdot j} + k_2 \tag{18}$$

where $w = 2\pi f$, f is the frequency, $k_{1,2}$ is the stiffness coefficient of the corresponding springs, η_1 is the fractional-damper coefficient, and α is the fractional order. According to the complex stiffness expression:

$$K^* = K + j \cdot wC \tag{19}$$

where K^* is the complex stiffness, K is the stiffness coefficient, and C is the damping coefficient. The stiffness and damping of the model are as follows:

$$\begin{aligned} K(w) &= \text{Real}(Z) \\ C(w) &= \text{Imag}(Z)/w \end{aligned} \tag{20}$$

where Real stands for the real part and Imag stands for the imaginary part. For the convenience of presentation:

$$\begin{aligned} a_1 &= k_1 + \eta_1 w^\alpha \cos(\frac{\pi}{2} \alpha) \\ b_1 &= \eta_1 w^\alpha \sin(\frac{\pi}{2} \alpha) \cdot j \\ c_1 &= k_1 \eta_1 w^\alpha \cos(\frac{\pi}{2} \alpha) \\ d_1 &= k_1 \eta_1 w^\alpha \sin(\frac{\pi}{2} \alpha) \cdot j \end{aligned} \tag{21}$$

The expressions of the stiffness and damping are obtained as follows:

$$\begin{aligned} k(w) &= k_2 + \frac{a_1 c_1 + b_1 d_1}{a_1^2 + b_1^2} \\ c(w) &= \left(\frac{a_1 d_1 - b_1 c_1}{a_1^2 + b_1^2} \right) / w \end{aligned} \tag{22}$$

Change the order α of the fractional-damper with the other parameters unchanged (keep $k_1 = 3 \times 10^6$ N/m, $k_2 = 160 \times 10^6$ N/m, $\eta_1 = 0.1 \times 10^6$ N·s/m). The stiffness and

damping of the model changing with the fractional order can be obtained. The maximum stiffness of the model decreases with the increase of the order, and the maximum stiffness peak appears when the order is greater than a certain degree, as shown in Figure 9a. As shown in Figure 9b, with the increase of the order, the low-frequency damping of the model becomes larger, showing obvious viscous characteristics.

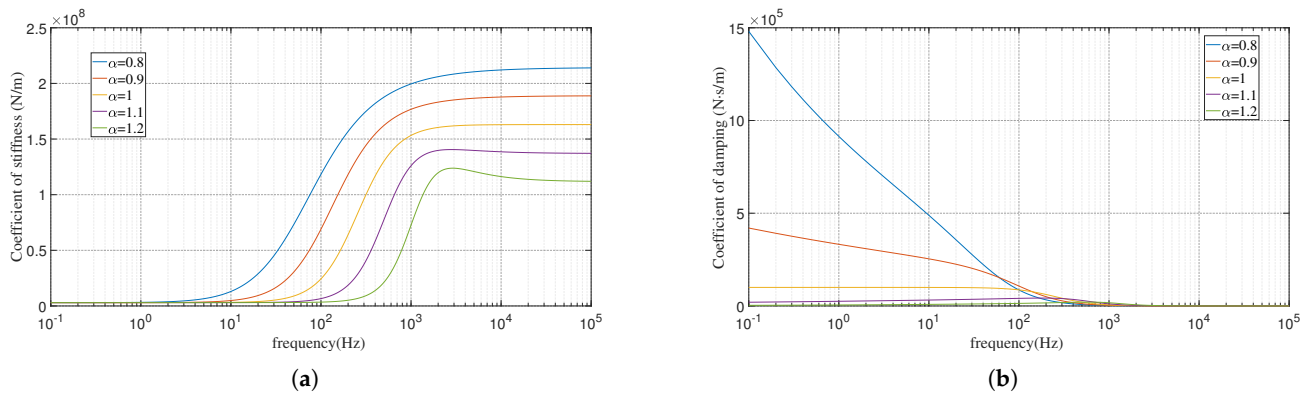


Figure 9. Effect of the fractional order on dynamic characteristics of the FOZGF model. (a) Change of dynamic stiffness with the α order. (b) Change of damping with the α order.

3.3.2. Fractional-Order Maxwell Gas Film Model

The structure of the fractional-order Maxwell gas film (FOMGF) model is shown in Figure 8b. The FOMGF model is obtained by replacing the damper of the Maxwell model with the fractional-damper. As for this model, we can obtain its transfer function expression by the Laplace transformation and Euler formula as follows:

$$Z = \frac{F(w)}{X(w)} = \frac{k_1\eta_1w^\alpha \cos(\frac{\pi}{2}\alpha) + k_1\eta_1w^\alpha \sin(\frac{\pi}{2}\alpha) \cdot j}{k_1 + \eta_1w^\alpha \cos(\frac{\pi}{2}\alpha) + \eta_1w^\alpha \sin(\frac{\pi}{2}\alpha) \cdot j} + \frac{k_2\eta_2w^\beta \cos(\frac{\pi}{2}\beta) + k_2\eta_2w^\beta \sin(\frac{\pi}{2}\beta) \cdot j}{k_2 + \eta_2w^\beta \cos(\frac{\pi}{2}\beta) + \eta_2w^\beta \sin(\frac{\pi}{2}\beta) \cdot j} + k_3 \quad (23)$$

where $w = 2\pi f$, f is the frequency, $k_{1,2,3}$ is the stiffness coefficient of the corresponding springs, $\eta_{1,2}$ is the fractional-damper coefficient, and α, β is the fractional order. For the convenience of presentation:

$$\begin{aligned} a_n &= k_n + \eta_n w^\theta \cos(\frac{\pi}{2}\theta) \\ b_n &= \eta_n w^\theta \sin(\frac{\pi}{2}\theta) \cdot j \\ c_n &= k_n \eta_n w^\theta \cos(\frac{\pi}{2}\theta) \\ d_n &= k_n \eta_n w^\theta \sin(\frac{\pi}{2}\theta) \cdot j \end{aligned} \quad (24)$$

where $\theta = \alpha$ when $n = 1$ and when $n = 2$, $\theta = \beta$. The expressions of the stiffness and damping of the model can be obtained from Equations (19) and (20) as follows:

$$\begin{aligned} k(w) &= k_3 + \frac{a_2c_2 + b_2d_2}{a_2^2 + b_2^2} + \frac{a_1c_1 + b_1d_1}{a_1^2 + b_1^2} \\ c(w) &= \left(\frac{a_2d_2 - b_2c_2}{a_2^2 + b_2^2} + \frac{a_1d_1 - b_1c_1}{a_1^2 + b_1^2} \right) / w \end{aligned} \quad (25)$$

Change the order α of the fractional-damper with the other parameters unchanged (keep $k_{1,2} = 3 \times 10^6$ N/m, $k_3 = 160 \times 10^6$ N/m, $\eta_{1,2} = 0.1 \times 10^6$ N·s/m, $\beta = 1$). As shown in Figure 10, the stiffness and damping of the model changing with the fractional order can be obtained. The main performance is that with the increase of the α value, the stiffness rising rate increases and the stiffness minimum peak appears. As the value of α changes, the damping characteristics change. At higher order, the damping first increases, then

decreases, and then stabilizes (damping peak). At low order, the damping decreases first and then stabilizes. The stiffness and damping expressions (Equation (25)) of the FOMGF model show that the effect of changing α and β is the same.

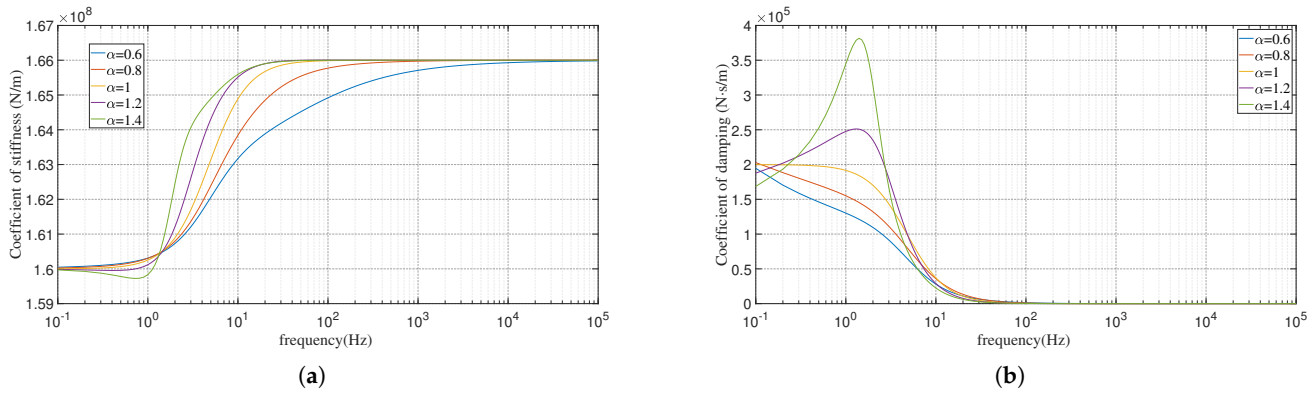


Figure 10. Effect of the fractional order on the dynamic characteristics of the FOMGF model. (a) Change of dynamic stiffness with the α order. (b) Change of damping with the α order.

3.3.3. Fractional-Order Three Parameter Gas Film Model

The structure of the fractional-order three-parameter gas film (FOTGF) model is shown in Figure 8c. The FOTGF model is obtained by replacing the damper of the three-parameter model with the fractional-damper. As for this model, it can be obtained by the Laplace transformation and Euler formula, where its transfer function expression is as follows:

$$Z = \frac{F(w)}{X(w)} = \frac{c + d \cdot j}{a + b \cdot j} \tag{26}$$

where a, b, c, d are equal to:

$$\begin{aligned} a &= k_1 + \eta_1 w^\alpha \cos\left(\frac{\pi}{2}\alpha\right) + \eta_2 w^\beta \cos\left(\frac{\pi}{2}\beta\right) \\ b &= \eta_1 w^\alpha \sin\left(\frac{\pi}{2}\alpha\right) + \eta_2 w^\beta \sin\left(\frac{\pi}{2}\beta\right) \\ c &= k_1 \eta_2 w^\beta \cos\left(\frac{\pi}{2}\beta\right) + \eta_1 \eta_2 w^{\alpha+\beta} \cos\left(\frac{\pi}{2}\alpha + \beta\right) \\ d &= k_1 \eta_2 w^\beta \sin\left(\frac{\pi}{2}\beta\right) + \eta_1 \eta_2 w^{\alpha+\beta} \sin\left(\frac{\pi}{2}\alpha + \beta\right) \end{aligned} \tag{27}$$

where $w = 2\pi f$, f is the frequency, k_1 are the stiffness coefficients of the corresponding springs, $\eta_{1,2}$ is the fractional-damper coefficient, and α, β is the fractional order. The expressions of the stiffness and damping of the model can be obtained from Equations (19) and (20) as follows:

$$\begin{aligned} k(w) &= \frac{ac + bd}{a^2 + b^2} \\ c(w) &= \left(\frac{ad - bc}{a^2 + b^2}\right) / w \end{aligned} \tag{28}$$

Change the order α of the fractional-damper with the other parameters unchanged (keep $k_1 = 160 \times 10^6$ N/m, $\eta_{1,2} = 0.1 \times 10^6$ N·s/m, $\beta = 1$). The stiffness and damping of the model changing with the fractional order can be obtained. The stiffness of the model changes in the middle- and high-frequency characteristics, especially in the high-frequency region. As shown in Figure 11a, when $\alpha < 1$, the high-frequency stiffness keeps rising. When $\alpha > 1$, the stiffness has an extreme peak, even a negative stiffness. The damping characteristic changes with the change of the α value, as shown in Figure 11b. At higher order, the damping first increases, then decreases, and then stabilizes (damping peak). At low order, the damping decreases first and then stabilizes.

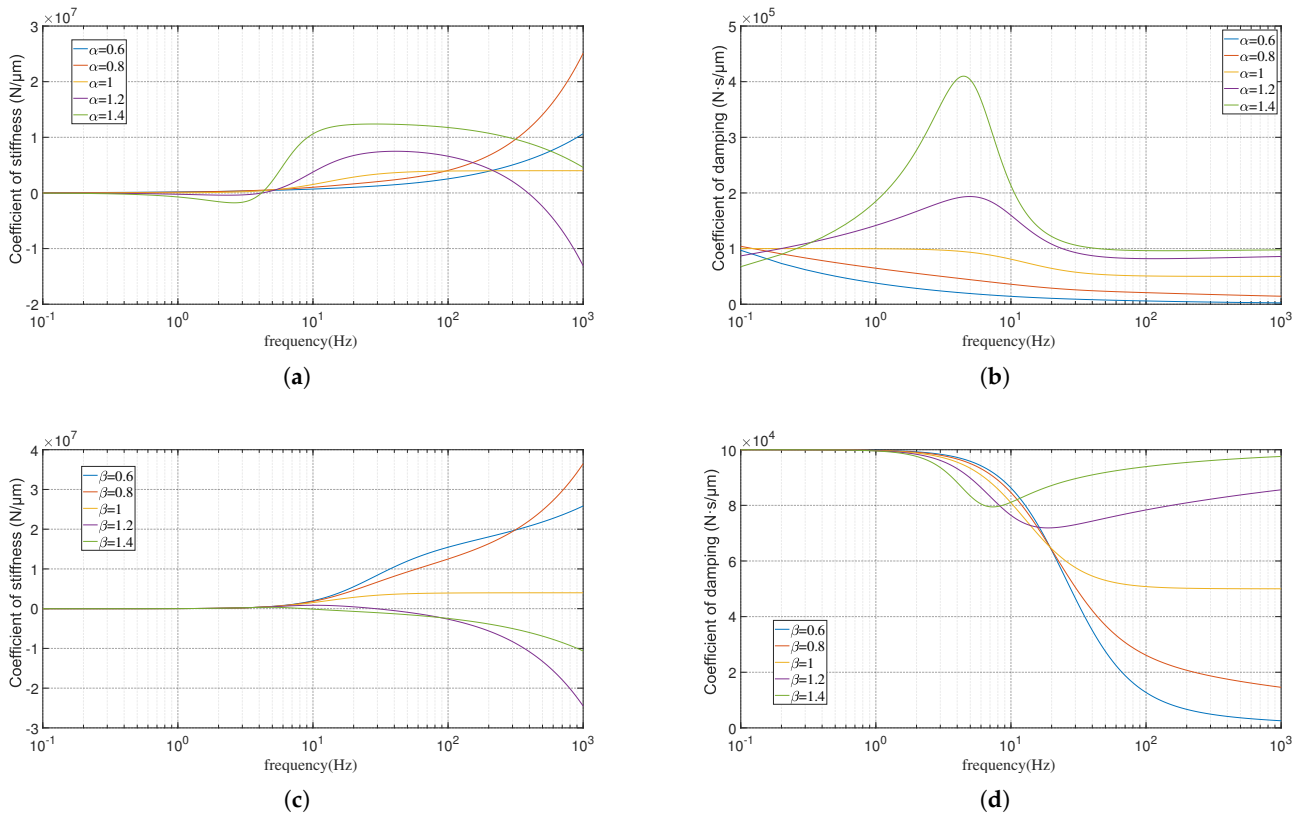


Figure 11. Effect of the fractional order on the dynamic characteristics of the FOTGF model. (a) Change of dynamic stiffness with the α order. (b) Change of damping with the α order. (c) Change of dynamic stiffness with the β order. (d) Change of damping with the β order.

Change the order β of the fractional-damper with the other parameters unchanged (keep $k_1 = 160 \times 10^6 \text{ N/m}$, $\eta_{1,2} = 0.1 \times 10^6 \text{ N}\cdot\text{s/m}$, $\alpha = 1$). The stiffness and damping of the model changing with the fractional order can be obtained. The stiffness of the model changes in the middle- and high-frequency characteristics, especially in the high-frequency region. As shown in Figure 11c, when $\beta < 1$, the high-frequency stiffness keeps rising. When $\beta > 1$, the stiffness has an extreme peak, even a negative stiffness. The damping characteristic changes with the change of β , as shown in Figure 11d. The main performance is that the high-frequency stable damping value increases with the increase of the order, and the damping minimum peak appears.

3.3.4. Fractional-Order Burgess Gas Film Model

The structure of the fractional-order Burgess gas film (FOBGF) model is shown in Figure 8c. The FOBGF model is obtained by replacing the damper of the Burgess model with the fractional-damper. As for this model, it can be obtained by the Laplace transformation and Euler formula. Make a, b, c, d as follows:

$$\begin{aligned}
 a &= k_1 k_2 + \eta_1 \eta_2 w^{\alpha+\beta} \cos\left(\frac{\pi}{2}(\alpha + \beta)\right) + (k_1 + k_2) \eta_1 w^\alpha \cos\left(\frac{\pi}{2}\alpha\right) + k_1 \eta_2 w^\beta \cos\left(\frac{\pi}{2}\beta\right) \\
 b &= \eta_1 \eta_2 w^{\alpha+\beta} \sin\left(\frac{\pi}{2}(\alpha + \beta)\right) + (k_1 + k_2) \eta_1 w^\alpha \sin\left(\frac{\pi}{2}\alpha\right) + k_1 \eta_2 w^\beta \sin\left(\frac{\pi}{2}\beta\right) \\
 c &= k_1 \eta_1 \eta_2 w^{\alpha+\beta} \cos\left(\frac{\pi}{2}(\alpha + \beta)\right) + k_1 k_2 \eta_1 w^\alpha \cos\left(\frac{\pi}{2}\alpha\right) \\
 d &= k_1 \eta_1 \eta_2 w^{\alpha+\beta} \sin\left(\frac{\pi}{2}(\alpha + \beta)\right) + k_1 k_2 \eta_1 w^\alpha \sin\left(\frac{\pi}{2}\alpha\right)
 \end{aligned}
 \tag{29}$$

where $w = 2\pi f$, f is the frequency, $k_{1,2}$ are the stiffness coefficients of the corresponding springs, $\eta_{1,2}$ is the fractional-damper coefficient, and α, β is the fractional order. The model transfer function is as follows:

$$Z = \frac{F(w)}{X(w)} = \frac{c + d \cdot j}{a + b \cdot j} \tag{30}$$

The expressions of the stiffness and damping of the model can be obtained from Equations (19) and (20) as follows:

$$k(w) = \frac{ac + bd}{a^2 + b^2}$$

$$c(w) = \left(\frac{ad - bc}{a^2 + b^2} \right) / w \tag{31}$$

Change the order α of the fractional-damper with the other parameters unchanged (keep $k_1 = 160 \times 10^5 \text{ N/m}$, $k_2 = 3 \times 10^5 \text{ N/m}$, $\eta_{1,2} = 0.1 \times 10^6 \text{ N}\cdot\text{s/m}$, $\beta = 1$). The stiffness and damping of the model changing with the fractional order can be obtained. As shown in Figure 12a, the characteristics of the model stiffness change in the intermediate frequency region. The main performance is that the stiffness rising rate increases with the increase of the value. As shown in Figure 12b, the damping characteristic changes with the change of the value. At higher order, the damping first increases, then decreases, then stabilizes, then increases, and finally, stabilizes. When the order is low, the damping decreases first and then stabilizes.

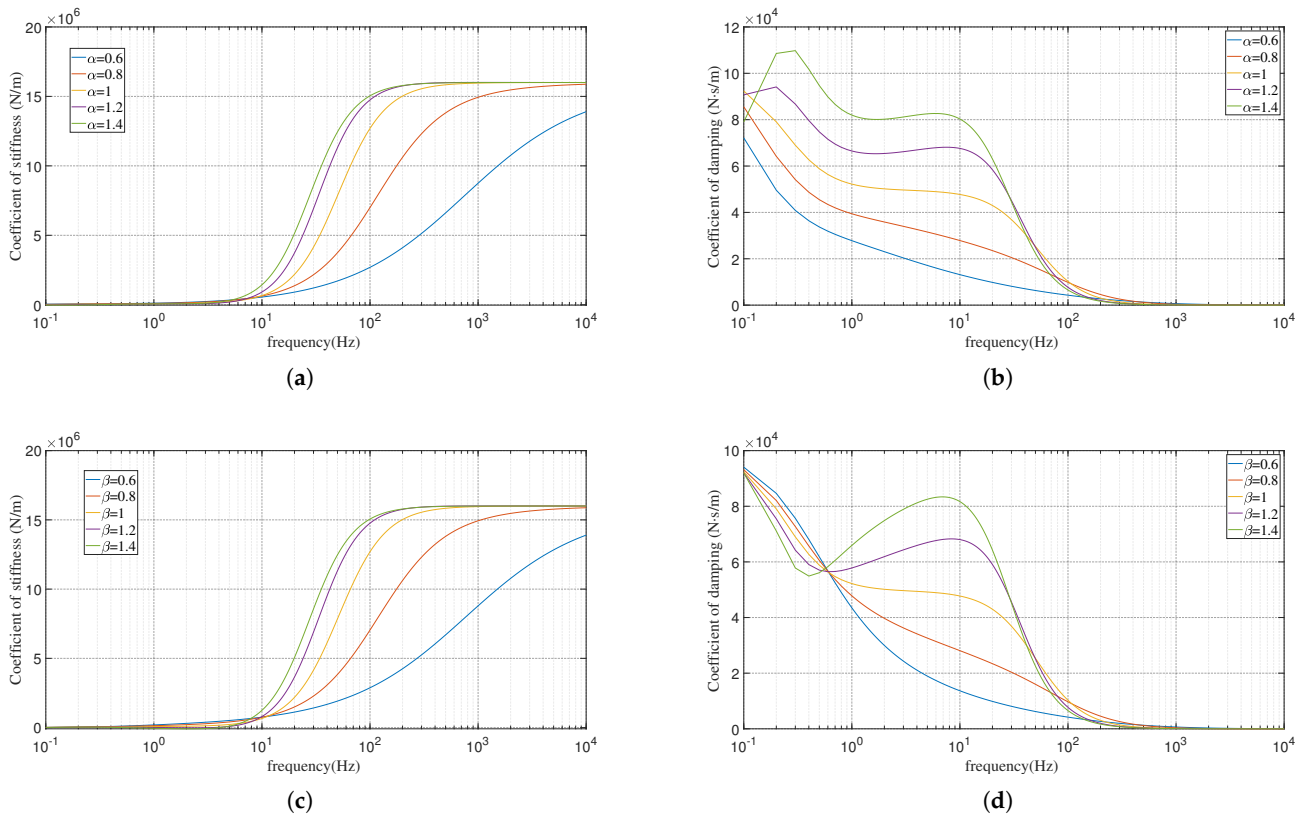


Figure 12. Effect of the fractional order on the dynamic characteristics of the FOBGF model. (a) Change of dynamic stiffness with the α order. (b) Change of damping with the α order. (c) Change of dynamic stiffness with the β order. (d) Change of damping with the β order.

Change the order β of the fractional-damper with the other parameters unchanged (keep $k_1 = 160 \times 10^5 \text{ N/m}$, $\eta_{1,2} = 0.1 \times 10^5 \text{ N}\cdot\text{s/m}$, $\alpha = 1$). The stiffness and damping of the model changing with the fractional order can be obtained. As shown in Figure 12c,

the stiffness change is similar to the change of α . As shown in Figure 12d, the damping characteristic changes with the change of the value of α . The low-frequency change of the damping characteristic is opposite to the change of α . The damping minimum peak appears. The change of the damping medium and high frequency is similar to the change of α .

4. Parameter Identification for the FOGF Models

In this paper, a variety of FOGF models are established. In order to identify the model parameters, a genetic algorithm-particle swarm optimization (GA-PSO) algorithm for parameter identification of the FOGF models was used [57,58].

The genetic algorithm (GA) is an algorithm that simulates the rules of the survival of the fittest in the process of biological evolution. It is widely used in optimization control and other fields [59,60]. The GA operator has selection, crossover, and mutation. The fitness function measures each individual's fitness to the environment, and each individual corresponds to a fitness value. The selection operator eliminates inferior individuals, and crossover and mutation produce new individuals. The population of individuals continues to evolve until the best individual is produced. Different from the PSO algorithm, the GA has a better global searching ability, but the GA cannot guarantee the accuracy of the solution.

The particle swarm optimization (PSO) algorithm simulates swarm behavior in nature. Each member (particle) in the swarm constantly changes its search mode by learning from its own experience and that of other members. Each particle calculates its speed and position according to Equation (32). Figure 13 is a diagram of the calculation equation. The PSO algorithm is widely used because of its simple implementation, high efficiency, and good robustness [61,62]. However, the PSO algorithm is suitable for dealing with optimization problems with high dimensions, multiple locally optimal solutions, and low requirements for the accuracy of the results. The PSO algorithm easily falls into local optima.

$$\begin{cases} v_{(i+1)d} = w \cdot v_{id} + c_{1d} \cdot (p_{id} - x_{id}) + c_2 \cdot (p_{gd} - x_{id}) \\ x_{(i+1)d} = x_{id} + v_{(i+1)d} \end{cases} \quad (32)$$

The GA and PSO algorithm are inspired by nature, and each has its advantages and disadvantages. To better identify the parameters of the FOGF system, this paper uses a parameter optimization method of the GA-PSO combined with a search. As shown in Figure 14, multiple groups of "global optimal values" are quickly searched by the GA, and then, the slow-speed search is carried out by the PSO algorithm. Ultimately, a more accurate global optimal value is searched around the "global optimal value".

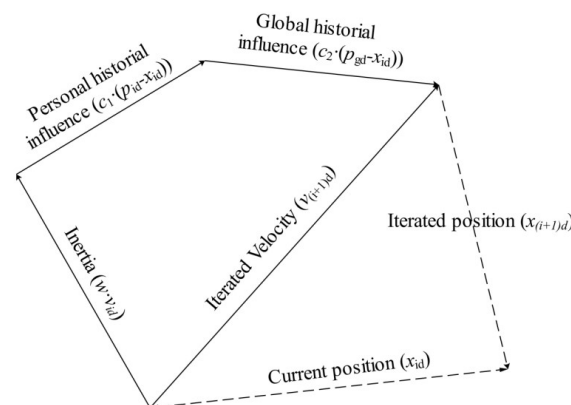


Figure 13. Schematic diagram of Equation (32).

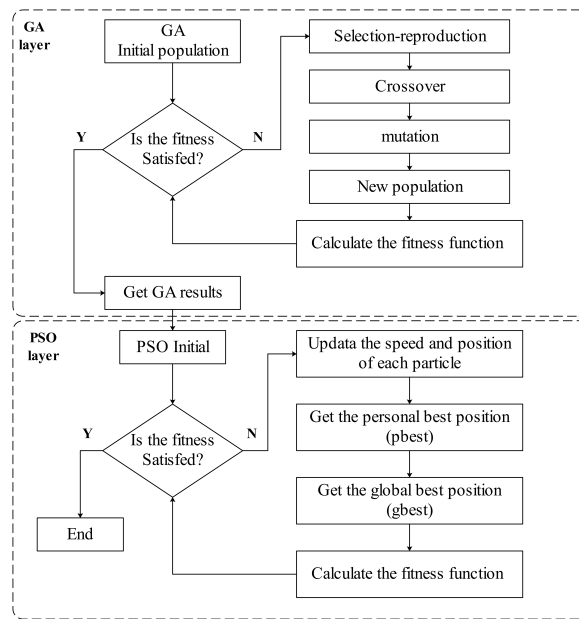


Figure 14. The GA-PSO iterative flow chart.

The GA-PSO algorithm was applied to the parameter identification of the FOGF system, and the root-mean-squared (RMS) error was introduced as the fitness function. The minimum RMS value was taken as the objective, and the model was iteratively identified. The RMS value was used to evaluate the modeling accuracy of the different models. The algorithm was considered convergent if the RMS value remained unchanged in many iterations (e.g., 50 iterations).

$$RMS = \sqrt{\frac{1}{n} \sum_{k=1}^n (|H_d(k) - H(k)|)^2} \tag{33}$$

where $H_d(k)$ is the experimentally measured transfer function value, $H(k)$ is the FOGF model value, and n is the data length.

5. Experimental Validation

5.1. FOGF Vibration Test System

In this paper, the transfer function of the gas film was evaluated by the vibration test, so as to verify the precision and accuracy of the established FOGF model. As shown in Figure 15, M is the mass, $F(w)$ is the external force, $K(w)$ is the system stiffness varying with frequency, and $C(w)$ is the system damping varying with frequency. The gas film mass system in this paper is a single-degree-of-freedom vibration system.

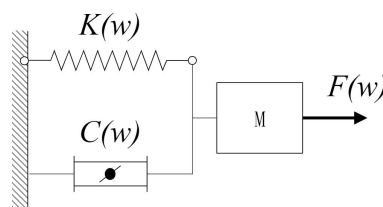


Figure 15. Single-degree-of-freedom vibration system.

In this single-degree-of-freedom system, the transfer function of the gas film vibration with the frequency dependency can be obtained as follows:

$$H_{af}(w) = \frac{A(w)}{F(w)} = \frac{-w^2}{k(w) - mw^2 + c(w)w \cdot j} \tag{34}$$

where $w = 2\pi f$, f is the frequency, m is the mass, $A(w)$ is the system acceleration frequency response, and $k(w)$ and $c(w)$ are the equivalent stiffness and damping in the FOGF model.

5.2. Experimental Platform

The experimental platform was an H-type air bearing floating motion platform, as shown in Figure 16a. We tested the dynamic characteristics of the gas film produced in the main X-direction. The y-direction mover of the platform forms the rigid mass ($m = 25.05$ Kg) of the FOGF vibration system in this setting and provides preload for the gas film.

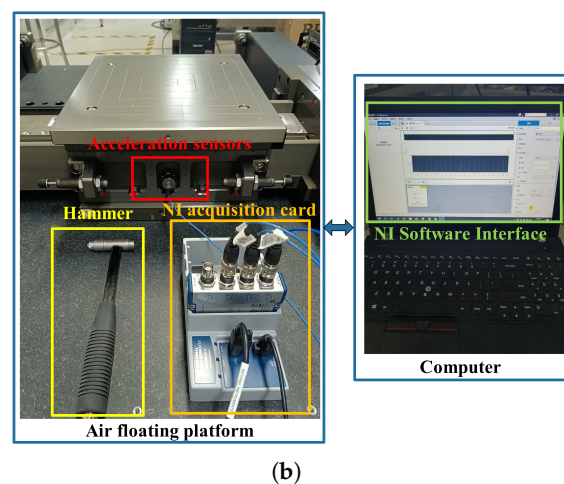
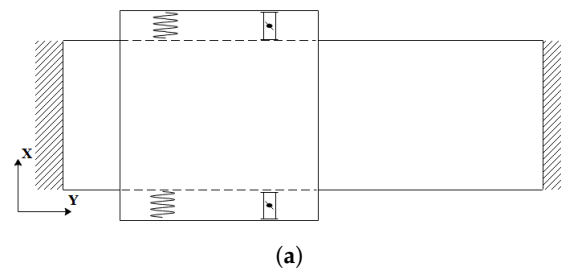


Figure 16. (a) Schematic diagram of the experimental platform. (b) Physical diagram of the air floating platform.

Impact testing is a low-cost and reliable test method [63]. Lin and Ali et al.'s experimental setup of the air bearing [64] and viscoelastic material [65–68] were implemented. Based on the actual situation of the experimental platform (Figure 16b), the impact testing experiment was applied to test the transfer function of the system. The hammer (PCB086C02) exerted force along the center of mass, and the response through the accelerometer (352B SN 244343) was measured. The data were collected by NI company's acquisition card (NI 9234) and processed by MATLAB (R2018b, MathWorks, Natick, MA, USA). The dynamic characteristics of the gas film were obtained by the fast Fourier transform (FFT) of the measured impact force and acceleration.

A similar impact force level was applied under the same condition (e.g., keep $P_s = 4.8$ MPa) to minimize the influence of the experimental conditions on the dynamic characteristics. Each experiment collected multiple data. In addition, the initial frequency response function and coherence function were checked to ensure the quality of the collected data.

5.3. Results and Discussion

After processing the experimental data, the critical frequency range data were intercepted. The repeatability of the data is shown in Figure 17. According to the experimental

data, the GA-PSO algorithm was used to identify the parameters of the proposed model. The transfer function of the gas film was obtained. The parameter identification results after convergence are shown in Table 1. The identification results are shown in Figure 18.

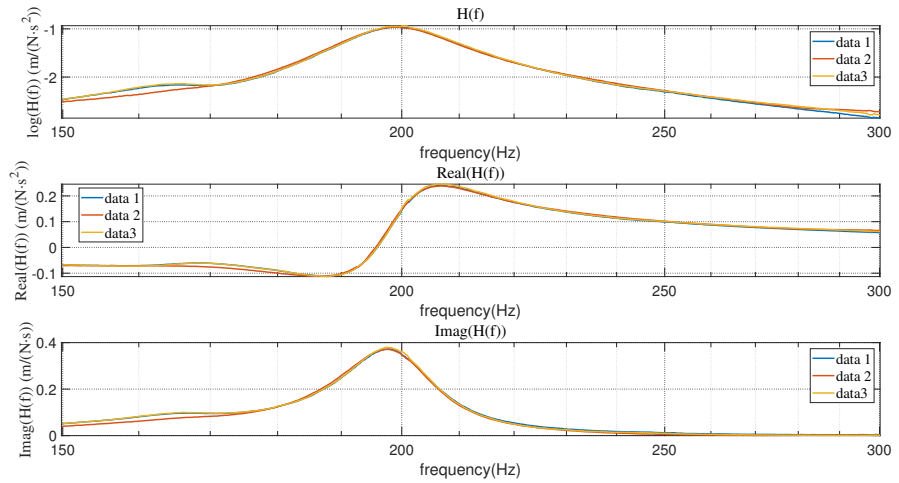


Figure 17. Schematic diagram of multiple groups of experimental data.

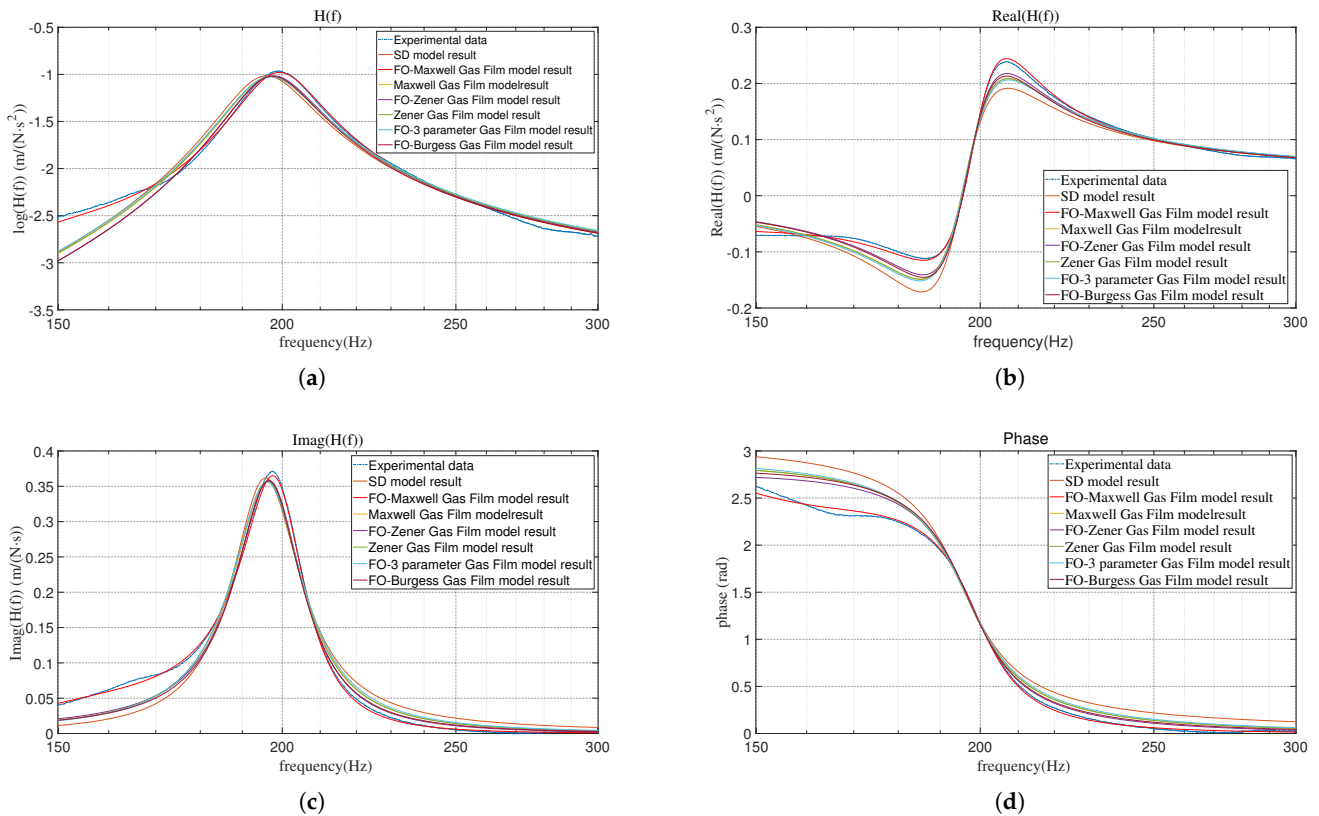


Figure 18. Comparison of the experimental results and model fitting results. (a) The logarithmic value of the transfer function H_{af} shown in Equation (34). (b) Real part of H_{af} . (c) Imaginary part of H_{af} . (d) Phase change of H_{af} .

Table 1. Parameter identification results of different models.

Model	Parameter Numbers	Identification Results (units: $k_{1,2,3}$ N/m, $\eta_{1,2}$ N·s/m)
SD model	2	$k = 3.78 \times 10^7, \eta = 3.45 \times 10^3$
FOZGF model	4	$k_1 = 3.20 \times 10^5, k_2 = 4.61 \times 10^9, \eta_1 = 4.33 \times 10^8, \alpha = 1.9186$
Zener model	3	$k_1 = 4.85 \times 10^4, k_2 = 3.81 \times 10^7, \eta_1 = 2.75 \times 10^5$
FOMGF model	7	$k_1 = 2.91 \times 10^6, k_2 = 4.89 \times 10^8, k_3 = 3.27 \times 10^7, \eta_1 = 16.14, \eta_2 = 101.81, \alpha = 1.7472, \beta = 0.1621$
Maxwell model	5	$k_1 = 3.53 \times 10^7, k_2 = 2.93 \times 10^6, k_3 = 1.09 \times 10^5, \eta_1 = 2.57 \times 10^5, \eta_2 = 5.19 \times 10^6$
FOTGF model	5	$k_1 = 2.00 \times 10^6, \eta_1 = 3.86 \times 10^7, \eta_2 = 1.14 \times 10^6, \alpha = 0.0036, \beta = 0.80$
FOBGF model	6	$k_1 = 4.05 \times 10^7, k_2 = 3.01 \times 10^8, \eta_1 = 1.75 \times 10^4, \eta_2 = 1.21 \times 10^5, \alpha = 1.3641, \beta = 0.0773$
TGF model	3	$k_1 = 2.13 \times 10^{10}, \eta_1 = 2.12 \times 10^4, \eta_2 = 4.259 \times 10^{10}$
BGF model	4	$k_1 = 9.95 \times 10^6, k_2 = 4.898 \times 10^{10}, \eta_1 = 4.84 \times 10^8, \eta_2 = 1.8 \times 10^8,$

Except for the three-parameter gas film model (TGF model) and Burgess gas film model (BGF model), the other models had certain effects on the equivalent fitting of the gas film. It can be seen from Figure 19 that the different models showed different capture effects. Due to the poor capture effect of the BGF model and TGF model, these two models are not added in Figures 18 and 19 so as not to affect the comparison of the other models. Table 2 shows the specific RMS values and compares the capture effects of different models with the standard spring–damping (SD) model as the standard error value.

$$E = \frac{\text{RMS}_{\text{SD}} - \text{RMS}_{\text{other}}}{\text{RMS}_{\text{SD}}} \times 100\% \quad (35)$$

$$E_m = \frac{e_{\text{SD}} - e_{\text{other}}}{e_{\text{SD}}} \times 100\%$$

where RMS_{SD} is the RMS value of the SD model, $\text{RMS}_{\text{other}}$ is the RMS value of the other models, E is the percentage of RMS reduction of the model relative to the standard spring damping model, e_{SD} is the peak error (maximum error) of the SD model, e_{other} is the peak error of the other models, E_m is the percentage of peak error reduction of the model compared with the standard spring damping model, and E and E_m show the improvement of the model capture accuracy. The larger E and E_m values of the model, the higher the capture accuracy of the model is.

Table 2. Error values of different models.

Model	RMS	E	Peak Error	E_m
SD model [31,32]	0.0016643	0.00%	0.06095	0.00%
FOZGF model	0.00092817	44.23%	0.03514	42.34%
Zener model [33,41]	0.0011119	33.19%	0.0392	35.70%
FOMGF model	0.00022979	86.19%	0.01041	82.91%
Maxwell model	0.0011131	33.12%	0.03948	35.22%
FOTGF model	0.0011844	28.83%	0.04209	31%
FOBGF model	0.0010477	37.05%	0.03826	37.23%
TGF model	0.0078358	−370.8%	0.3560	−484.09%
BGF model	0.0082992	−398.6%	0.3717	−509.8%

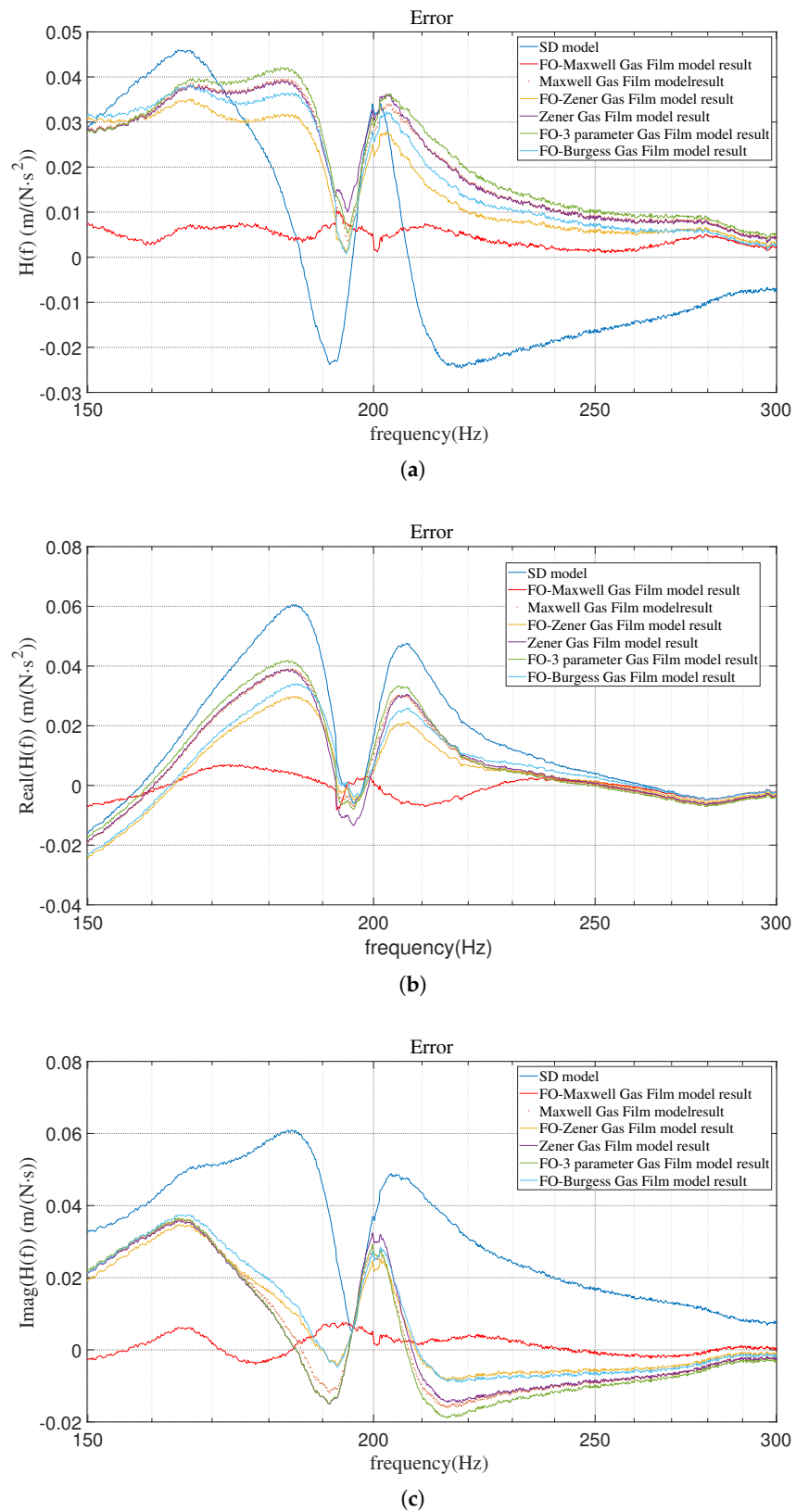


Figure 19. Comparison of the fitting errors between different models. (a) Error value of transfer function H_{af} . (b) Error value of the real part. (c) Error value of the imaginary part.

For the experimental platform in this paper, the capture effects of different models were sorted from best to worst as follows: FOMGF model ($E = 86.19\%$, $E_m = 82.91\%$),

FOZGF model ($E = 44.23\%$, $E_m = 42.34\%$), FOBGF model ($E = 37.05\%$, $E_m = 37.23\%$), Zener model ($E = 33.19\%$, $E_m = 35.70\%$), Maxwell model ($E = 33.12\%$, $E_m = 35.22\%$), FOTGF model ($E = 28.83\%$, $E_m = 31\%$), SD model ($E = 0\%$, $E_m = 0\%$), TGF model ($E = -370.8\%$, $E_m = -484.09\%$), BGF model ($E = -398.6\%$, $E_m = -509.8\%$). The FOGF model as a whole had a smaller RMS value and a smaller maximum error value, and the traditional Zener model and Maxwell model also had a better effect. The FOMGF model had the best performance, and the capture effect was obviously improved. The capture ability of the BGF model and TGF model was far lower than that of the SD model, and the model results were greatly optimized after the introduction of the fractional-damper. The 4-parameter FOZGF model was better than the 5-parameter Maxwell model. The results of the 3-parameter Zener model and 5-parameter Maxwell model had little difference, which shows that simply adding parameters without introducing the fractional order may have a limited effect.

The gas film characteristic curve in Section 2 shows that the film had the minimum stiffness peak and almost no maximum stiffness peak. The maximum peak of film damping was not obvious. In most cases, the damping changed to decreasing first, then stabilizing, and then, decreasing. In the characteristic curve of the FOMGF model in Section 3, the model had the minimum stiffness peak when the order was changed (change α while $\beta = 1$, and vice versa). With the change of the order, the damping trend of the model can change from a monotonic decrease to the maximum damping peak. The other FOGF models had some characteristics that the gas film may not have. For example, the FOBGF model had the minimum damping peak, while the FOZGF model may have a stiffness maximum peak and no stiffness minimum peak. The characteristics of the FOMGF model changing with the order can better capture the gas film characteristics in general than the other models. The experimental results in Section 5 also show this discussion. Some gas film characteristics cannot be captured by the traditional models, but can be captured by the FOGF models. With the introduction of the fractional order, the FOGF model had better results than the corresponding traditional model. The FOGF models had a more complex implementation form than the traditional models. This gives the FOGF model higher universality and accuracy in the equivalent process.

6. Conclusions

In this paper, the FOGF model was introduced into the research field of the dynamic characteristics of the gas film. Four FOGF models were established: FOZGF model, FOMGF model, FOTGF model, and FOBGF model. The influence of the fractional order on the dynamic characteristics of these four models was obtained by simulation. The FOGF models had more complex dynamic characteristics than the traditional equivalent models. Based on the complex characteristics of the gas film in practice, the FOGF models can better and more accurately capture the dynamic characteristics of the gas film in theory.

The existing models (spring-damper model, Zener model, Maxwell model, etc.) and the established FOGF models were identified by the GA-PSO algorithm, and the parameter estimation results of the different models were given. The experimental results showed that the FOGF models can capture the film characteristics more accurately than the traditional models. The FOGF models of different air floating platforms had different effects. The FOMGF model had the best performance on this experimental platform. This paper can provide a convenient and effective idea for the control modeling of air-bearing-related fields (such as ultra-precision motion platforms). The proposed method captures the characteristics of the existing air floating platform and cannot guide the design of the air floating platform. The FOGF model is beneficial to further expanding the application of fractional-order theory in engineering. In future research, the FOGF model is expected to improve the air floating platform's real-time vibration control and suppression effect in the motion control process.

Author Contributions: Ideas, software, validation, investigation, writing, comments and editing: X.T. and Y.L. Review, commentary: B.H. All authors have read and agreed to the published version of the manuscript.

Funding: This work was supported by the National Natural Science Foundation of China (51975234).

Data Availability Statement: Not applicable.

Conflicts of Interest: The authors declare no conflict of interest.

References

1. Powell, J. *Design of Aerostatic Bearings*; Machinery Pub. Co: Brighton, UK, 1970; pp. 89–99.
2. Geng, Y.; Wang, Y.; Yan, Y.; Zhao, X. A novel AFM-based 5-axis nanoscale machine tool for fabrication of nanostructures on a micro ball. *Rev. Sci. Instruments* **2017**, *88*, 115109. [[CrossRef](#)]
3. Chen, G.; Sun, Y.; Zhang, F.; An, C.; Chen, W.; Su, H. Influence of ultra-precision flycutting spindle error on surface frequency domain error formation. *Int. J. Adv. Manuf. Technol.* **2017**, *88*, 3233–3241. [[CrossRef](#)]
4. Krijnen, M.E.; van Ostayen, R.A.; HosseinNia, H. The application of fractional-order control for an air-based contactless actuation system. *ISA Trans.* **2018**, *82*, 172–183. [[CrossRef](#)]
5. Bos, E.; Moers, T.; Van Riel, M. Design and verification of an ultra-precision 3D-coordinate measuring machine with parallel drives. *Meas. Sci. Technol.* **2015**, *26*, 085904. [[CrossRef](#)]
6. Jayson, E.M.; Murphy, J.; Smith, P.; Talke, F.E. Effects of air bearing stiffness on a hard disk drive subject to shock and vibration. *J. Trib.* **2003**, *125*, 343–349. [[CrossRef](#)]
7. Yu, S.; Liu, B.; Hua, W.; Zhou, W. Contact Induced Off-Track Vibrations of Air Bearing-Slider-Suspension System in Hard Disk Drives. *Proc. Int. Jt. Tribol. Conf.* **2006**, 42592, 891–898.
8. Harrison, W. *The Hydrodynamical Theory of Lubrication with Special Reference to Air as a Lubricant*; Cambridge University Press: Cambridge, UK, 1913.
9. Bhat, N.; Kumar, S.; Tan, W.; Narasimhan, R.; Low, T.C. Performance of inherently compensated flat pad aerostatic bearings subject to dynamic perturbation forces. *Precis. Eng.* **2012**, *36*, 399–407. [[CrossRef](#)]
10. Charki, A.; Diop, K.; Champmartin, S.; Ambari, A. Numerical simulation and experimental study of thrust air bearings with multiple orifices. *Int. J. Mech. Sci.* **2013**, *72*, 28–38. [[CrossRef](#)]
11. Gao, Q.; Qi, L.; Gao, S.; Lu, L.; Song, L.; Zhang, F. A FEM based modeling method for analyzing the static performance of aerostatic thrust bearings considering the fluid-structure interaction. *Tribol. Int.* **2021**, *156*, 106849. [[CrossRef](#)]
12. Wang, X.; Xu, Q.; Wang, B.; Zhang, L.; Yang, H.; Peng, Z. Effect of surface waviness on the static performance of aerostatic journal bearings. *Tribol. Int.* **2016**, *103*, 394–405. [[CrossRef](#)]
13. Heshmat, H.; Walton, J.F. Starved Hydrodynamic Gas Foil Bearings—Experiment, Micromechanical Phenomenon, and Hypotheses. *J. Tribol.* **2016**, *138*, 041703. [[CrossRef](#)]
14. San Andrés, L.; Yang, J.; Devitt, A. On Tilting Pad Carbon–Graphite Porous Journal Bearings: Measurements of Imbalance Response and Comparison to Predictions of Bearing Performance and System Dynamic Response. *Tribol. Trans.* **2021**, *64*, 981–995. [[CrossRef](#)]
15. Mallisetty, P.K.; Samanta, P.; Murmu, N. Nonlinear transient analysis of rigid rotor mounted on externally pressurized double-layered porous gas journal bearings accounting velocity slip. *J. Braz. Soc. Mech. Sci. Eng.* **2020**, *42*, 1–12. [[CrossRef](#)]
16. Wu, Y.; Deng, M.; Feng, K.; Guan, H.; Cao, Y. Investigations on the nonlinear dynamic characteristics of a rotor supported by porous tilting pad bearings. *Nonlinear Dyn.* **2020**, *100*, 2265–2286. [[CrossRef](#)]
17. Durazo-Cardenas, I.; Corbett, J.; Stephenson, D.J. Permeability and dynamic elastic moduli of controlled porosity ultra-precision aerostatic structures. *Ceram. Int.* **2014**, *40*, 3041–3051. [[CrossRef](#)]
18. Kang, T.S.; Choi, D.H.; Jeong, T.G. Optimal design of HDD air-lubricated slider bearings for improving dynamic characteristics and operating performance. *J. Trib.* **2001**, *123*, 541–547. [[CrossRef](#)]
19. Cui, H.; Wang, Y.; Yue, X.; Huang, M.; Wang, W. Effects of manufacturing errors on the static characteristics of aerostatic journal bearings with porous restrictor. *Tribol. Int.* **2017**, *115*, 246–260. [[CrossRef](#)]
20. Chang-Jian, C.W. Chaotic response and bifurcation analysis of a flexible rotor supported by porous and non-porous bearings with nonlinear suspension. *Nonlinear Anal. Real World Appl.* **2009**, *10*, 1114–1138. [[CrossRef](#)]
21. Panzera, T.; Rubio, J.; Bowen, C.; Walker, P. Microstructural design of materials for aerostatic bearings. *Cem. Concr. Compos.* **2008**, *30*, 649–660. [[CrossRef](#)]
22. Park, D.J.; Kim, C.H.; Jang, G.H.; Lee, Y.B. Theoretical considerations of static and dynamic characteristics of air foil thrust bearing with tilt and slip flow. *Tribol. Int.* **2008**, *41*, 282–295. [[CrossRef](#)]
23. Ishibashi, K.; Kondo, A.; Kawada, S.; Miyatake, M.; Yoshimoto, S.; Stolarski, T. Static and dynamic characteristics of a downsized aerostatic circular thrust bearing with a single feed hole. *Precis. Eng.* **2019**, *60*, 448–457. [[CrossRef](#)]
24. Maamari, N.; Krebs, A.; Weikert, S.; Wild, H.; Wegener, K. Stability and dynamics of an orifice based aerostatic bearing with a compliant back plate. *Tribol. Int.* **2019**, *138*, 279–296. [[CrossRef](#)]

25. Yoshimoto, S.; Kohno, K. Static and dynamic characteristics of aerostatic circular porous thrust bearings (effect of the shape of the air supply area). *J. Tribol.* **2001**, *123*, 501–508. [[CrossRef](#)]
26. Oiwa, N.; Masuda, M.; Hirayama, T.; Matsuoka, T.; Yabe, H. Deformation and flying height orbit of glass sheets on aerostatic porous bearing guides. *Tribol. Int.* **2012**, *48*, 2–7. [[CrossRef](#)]
27. Jia, C.; Pang, H.; Ma, W.; Qiu, M. Analysis of dynamic characteristics and stability prediction of gas bearings. *Ind. Lubr. Tribol.* **2017**, *69*, 123–130. [[CrossRef](#)]
28. Fourka, M.; Tian, Y.; Bonis, M. Prediction of the stability of air thrust bearings by numerical, analytical and experimental methods. *Wear* **1996**, *198*, 1–6. [[CrossRef](#)]
29. Plante, J.S.; Vogan, J.; El-Aguizy, T.; Slocum, A.H. A design model for circular porous air bearings using the 1D generalized flow method. *Precis. Eng.* **2005**, *29*, 336–346. [[CrossRef](#)]
30. Geerts, N. Linear Dynamic Analysis of Rotorsystems with gAs Bearings. Master's Thesis, Eindhoven University of Technology, Eindhoven, The Netherlands, 1995.
31. Sun, Y.; Zeng, L.; Luo, Y.; Li, X. Model Decoupled Synchronization Control Design with Fractional Order Filter for H-Type Air Floating Motion Platform. *Entropy* **2021**, *23*, 633. [[CrossRef](#)]
32. Jiang, W.; Jia, W.C.; Liu, S.S.; Hu, Y.T.; Hu, H.P. Roll Vibration Analysis of Planar Aerostatic Bearings through a Distributed Spring Model. In *Advanced Materials Research*; Trans Tech Publications Ltd.: Bäch, Switzerland, 2012; Volume 346, pp. 332–338.
33. Arghir, M.; Matta, P. Compressibility effects on the dynamic characteristics of gas lubricated mechanical components. *Comptes Rendus Mécanique* **2009**, *337*, 739–747. [[CrossRef](#)]
34. Al-Bender, F. On the modeling of the dynamic characteristics of aerostatic bearing films: From stability analysis to active compensation. *Precis. Eng.* **2009**, *33*, 117–126. [[CrossRef](#)]
35. Sahraoui, S.; Zekri, N. On fractional modeling of viscoelastic foams. *Mech. Res. Commun.* **2019**, *96*, 62–66. [[CrossRef](#)]
36. Liang, Y.; Guan, P. Improved Maxwell model with structural dashpot for characterization of ultraslow creep in concrete. *Constr. Build. Mater.* **2022**, *329*, 127181. [[CrossRef](#)]
37. Hinze, M.; Xiao, S.; Schmidt, A.; Nowak, W. Experimental evaluation and uncertainty quantification for a fractional viscoelastic model of salt concrete. *Mech. -Time-Depend. Mater.* **2022**, 1–24. [[CrossRef](#)]
38. Sánchez, E.; Nájera, A.; Sotomayor, O. Numerical study of the viscoelastic mechanical response of polystyrene in the process of thermoforming through the generalized Maxwell model. *Mater. Today Proc.* **2022**, *49*, 107–114. [[CrossRef](#)]
39. Nadzharyan, T.; Kostrov, S.; Stepanov, G.; Kramarenko, E.Y. Fractional rheological models of dynamic mechanical behavior of magnetoactive elastomers in magnetic fields. *Polymer* **2018**, *142*, 316–329. [[CrossRef](#)]
40. Alcoutlabi, M.; Martinez-Vega, J. Application of fractional calculus to viscoelastic behavior modeling and to the physical ageing phenomenon in glassy amorphous polymers. *Polymer* **1998**, *39*, 6269–6277. [[CrossRef](#)]
41. Zhu, J. *Dynamic Characteristics and Nano-Vibration of Aerostatic Bearings*; Hua Zhong University of Science and Technology: Wuhan, China, 2014.
42. Wei, L. Study on Loading Characteristics of Orifice Compensated Aerostatic Thrust Bearing. Ph.D. Thesis, Harbin Institute of Technology, Harbin, China, 2010.
43. Petráš, I. *Fractional-Order Nonlinear Systems: Modeling, Analysis and Simulation*; Springer Science & Business Media: Berlin/Heidelberg, Germany, 2011.
44. Nabi, K.N.; Abboubakar, H.; Kumar, P. Forecasting of COVID-19 pandemic: From integer derivatives to fractional derivatives. *Chaos Solitons Fractals* **2020**, *141*, 110283. [[CrossRef](#)]
45. Shymanskyi, V.; Sokolovskyy, Y. Finite Element Calculation of the Linear Elasticity Problem for Biomaterials with Fractal Structure. *Open Bioinform. J.* **2021**, *14*, 114–122. [[CrossRef](#)]
46. Wu, J.; Wang, L.; Li, L.; Shu, Y.; Yang, L.; Lei, T. Sliding State Analysis of Fractal Rough Interface Based on the Finite Element Method. *Materials* **2021**, *14*, 2121. [[CrossRef](#)]
47. Shymanskyi, V.; Sokolovskyy, Y.; Boretska, I.; Sokolovskyy, I.; Markelov, O.; Storozhuk, O. Application of FEM with Piecewise Mittag-Leffler Functions Basis for the Linear Elasticity Problem in Materials with Fractal Structure. In Proceedings of the 2021 IEEE XVIIth International Conference on the Perspective Technologies and Methods in MEMS Design (MEMSTECH), Polyana (Zakarpattya), Ukraine, 12–16 May 2021; pp. 16–19.
48. Shymanskyi, V.; Sokolovskyy, Y. Variational Method for Solving the Viscoelastic Deformation Problem in Biomaterials with Fractal Structure. In Proceedings of the IT&I, Kyiv, Ukraine, 1–3 December 2021; pp. 125–134.
49. Lischke, A.; Zayernouri, M.; Zhang, Z. Spectral and spectral element methods for fractional advection–diffusion–reaction equations. *Handb. Fract. Calc. Appl. Numer. Methods* **2019**, *3*, 157–183.
50. Shah, F.A.; Abass, R.; Debnath, L. Numerical solution of fractional differential equations using Haar wavelet operational matrix method. *Int. J. Appl. Comput. Math.* **2017**, *3*, 2423–2445. [[CrossRef](#)]
51. Li, X. Numerical solution of fractional differential equations using cubic B-spline wavelet collocation method. *Commun. Nonlinear Sci. Numer. Simul.* **2012**, *17*, 3934–3946. [[CrossRef](#)]
52. Torge, M.; Bottlender, R.; Strauß, A.; Möller, H. Numerische klassifikation psychopathologischer daten mittels der logistischen Regression. *Eur. Psychiatry* **1998**, *13*, 321s.
53. Podlubny, I. *Fractional Differential Equations, Mathematics in Science and Engineering*; Academic Press: New York, NY, USA, 1999.

54. Caputo, M. Linear models of dissipation whose Q is almost frequency independent—II. *Geophys. J. Int.* **1967**, *13*, 529–539. [[CrossRef](#)]
55. Oustaloup, A.; Moreau, X.; Nouillant, M. The CRONE suspension. *Control Eng. Pract.* **1996**, *4*, 1101–1108. [[CrossRef](#)]
56. Chen, B.; Li, C.; Wilson, B.; Huang, Y. Fractional modeling and analysis of coupled MR damping system. *IEEE/CAA J. Autom. Sin.* **2016**, *3*, 288–294.
57. Premalatha, K.; Natarajan, A. Hybrid PSO and GA for global maximization. *Int. J. Open Probl. Compt. Math* **2009**, *2*, 597–608.
58. He, P.; Fang, Q.; Jin, H.; Ji, Y.; Gong, Z.; Dong, J. Coordinated design of PSS and STATCOM-POD based on the GA-PSO algorithm to improve the stability of wind-PV-thermal-bundled power system. *Int. J. Electr. Power Energy Syst.* **2022**, *141*, 108208. [[CrossRef](#)]
59. Kumar, M.; Husain, D.; Upreti, N.; Gupta, D. Genetic Algorithm: Review and Application. 2010. Available online: <https://ssrn.com/abstract=3529843> (accessed on 16 June 2022).
60. Katoch, S.; Chauhan, S.S.; Kumar, V. A review on genetic algorithm: Past, present, and future. *Multimed. Tools Appl.* **2021**, *80*, 8091–8126. [[CrossRef](#)]
61. Marini, F.; Walczak, B. Particle swarm optimization (PSO). A tutorial. *Chemom. Intell. Lab. Syst.* **2015**, *149*, 153–165. [[CrossRef](#)]
62. De Oca, M.A.M.; Stutzle, T.; Birattari, M.; Dorigo, M. Frankenstein’s PSO: A composite particle swarm optimization algorithm. *IEEE Trans. Evol. Comput.* **2009**, *13*, 1120–1132. [[CrossRef](#)]
63. Siewert, T.A.; Manahan, M.; McCowan, C.N.; Holt, J.; Marsh, F.; Ruth, E. The history and importance of impact testing. *ASTM Spec. Tech. Publ.* **2000**, *1380*, 3–16.
64. Ali, N.; García, J. Experimental studies on the dynamic characteristics of rolling element bearings. *Proc. Inst. Mech. Eng. Part J J. Eng. Tribol.* **2010**, *224*, 659–666. [[CrossRef](#)]
65. Lin, T.R.; Farag, N.H.; Pan, J. Evaluation of frequency dependent rubber mount stiffness and damping by impact test. *Appl. Acoust.* **2005**, *66*, 829–844. [[CrossRef](#)]
66. Tang, Z.; Pillay, P.; Omekanda, A.M. Vibration prediction in switched reluctance motors with transfer function identification from shaker and force hammer tests. *IEEE Trans. Ind. Appl.* **2003**, *39*, 978–985. [[CrossRef](#)]
67. Zhou, J.; Zhang, C.; Wang, Z.; Mao, K. Study on dynamic characteristics of the disc spring system in vibration screen. *Shock Vib.* **2020**, *2020*, 3518037. [[CrossRef](#)]
68. Dou, Y.; Wang, P.; Ding, W.; Wang, S.; Wei, K. Effect of viscoelastic-plastic dynamic properties of rail pads on curved rail dynamic characteristics based on the modified SEM–SM hybrid method. *Veh. Syst. Dyn.* **2022**, 1–25. [[CrossRef](#)]